Li et al. *NPG Asia Materials* (2018) 10: 406–416
DOI 10.1038/s41427-018-0042-5

NPG Asia Materials

ARTICLE Open Access

Holey graphene-wrapped porous $TiNb_{24}O_{62}$ microparticles as high-performance intercalation pseudocapacitive anode materials for lithium-ion capacitors

Shaohui Li[1], Jingwei Chen[1], Xuefei Gong[1], Jiangxin Wang[1] and Pooi See Lee[1]

Abstract

It is desirable to develop an energy storage system with both high energy density and high power density along with excellent cycling stability to meet practical application requirements. Lithium-ion capacitors (LICs) are very promising due to the combined merits of the high power density of electrochemical capacitors and the high energy density of batteries. However, the lack of high rate performance anode materials has been the major challenge of lithium-ion capacitors. Herein, we designed and synthesized holey graphene-wrapped porous $TiNb_{24}O_{62}$ as an anode material for lithium-ion capacitors. Pseudocapacitive storage behaviors with fast kinetics, high reversibility, and excellent cycling stability were demonstrated. The hybrid material can deliver a high capacity of 323 mAh g^{-1} at 0.1 A g^{-1}, retaining 183 mAh g^{-1} at 10 A g^{-1}. Coupled with a carbon nanosheet-based cathode, an LIC with an ultrahigh energy density of 103.9 Wh kg^{-1} was obtained, and it retained 28.9 Wh kg^{-1} even under a high power density of 17.9 kW kg^{-1} with a high capacity retention of 81.8% after 10,000 cycles.

Introduction

With increasing demand for consumer electronics, electronic vehicles (EVs) and hybrid electric vehicles (HEVs), energy storage systems that possess both high energy and high power density as well as long-term stability have attracted more interest in recent years[1–3]. Lithium-ion batteries (LIBs) and supercapacitors (SCs) have been extensively studied in the past decades to meet the requirements of consumer electronics, such as mobile phones, computers, and cameras[4–6]. Unfortunately, while LIBs can deliver high energy density, they are limited by low power density and poor cycling stability. Compared with LIBs, SCs exhibit high power density, a long cycling life, and fast charge/discharge processes while suffering from limited energy density. In view of these drawbacks, LIBs and SCs are not yet able to satisfy the practical application requirements of some electronic devices, EVs and HEVs. Therefore, an energy storage system that can provide both high energy and high power density is very attractive and urgently needed.

Recently, as a new type of energy storage system, LICs have attracted increasing attention by bridging the gap between LIBs and SCs, and they can deliver higher power than LIBs and more energy than SCs[7,8]. Usually, LICs consist of an LIB-type anode and a capacitor-type cathode in an Li-salt-containing organic electrolyte. To date, some LICs have been explored by using LIB anode materials, such as $Li_4Ti_5O_{12}$/C nanofiber//carbon nanofiber[7], Sn/N-rich nanotube//N-rich nanotube[8], Fe_3O_4/graphene//3D graphene[9], and $ZnMn_2O_4$/graphene//N-doped carbon nanosheets[10], and they have exhibited exciting

Correspondence: Pooi See. Lee (pslee@ntu.edu.sg)
[1]School of Materials Science and Engineering, Nanyang Technological University, Singapore 639798, Singapore

results. However, most of these hybrid systems using conversion-type or alloy-type nanostructured anode materials operate at low potentials (~0.5 V vs Li/Li^+) and are prone to electrolyte reduction and formation of thick solid-electrolyte interphase (SEI) layers, leading to limited rate capabilities, poor cycling lives, and safety issues. Compared with conversion-type and alloy-type anode materials, intercalation-type materials are more attractive for LICs due to their superior cycling stability, higher first-cycle coulombic efficiency, and faster charge/discharge rate performance, showing their promise for use in EVs/HEVs[3,4]. $Li_4Ti_5O_{12}$ is a typical zero-strain intercalation-type anode material and has been intensively studied[11–13]. The high working potential (~1.57 V vs Li/Li^+) can effectively inhibit the formation of SEI layers/lithium dendrites with negligible volume change (<0.2%) during lithiation/delithiation processes, making it a perfect candidate as an anode material with outstanding cycling stability and high safety. Good rate capability $Li_4Ti_5O_{12}$-based materials have been achieved by modifying the structure, combining with carbon materials and controlling the particle sizes[7,12]. However, the main problem of this material is its low theoretical capacity of 175 mAh g^{-1}, which results in poor energy density. Therefore, to fulfill the practical application requirements of EVs, it is crucial to explore novel anode materials that have larger capacities without compromising the cycling stability and safety properties of $Li_4Ti_5O_{12}$.

More recently, mixed-metal oxides of $Ti_xNb_yO_z$, such as $TiNb_2O_7$ and $Ti_2Nb_{10}O_{29}$, have been regarded as promising candidates for high-rate-capability and high-energy-density LIBs anode material, and they have similar working potentials to that of $Li_4Ti_5O_{12}$ and possess higher theoretical capacities of 388 and 396 mAh g^{-1} due to multiple Ti^{3+}/Ti^{4+}, Nb^{3+}/Nb^{4+}, and Nb^{4+}/Nb^{5+} redox couples, respectively[6,14,15]. The theoretical capacities surpass those of other titanium- and niobium-based anodes, such as bronze TiO_2 (335 mAh g^{-1})[16,17], $Li_4Ti_5O_{12}$ (175 mAh g^{-1})[11,18], and orthorhombic Nb_2O_5 (200 mAh g^{-1})[19–21]. In addition, the high Li^+ storage potential (~1.7 V) can also ensure safe operation by avoiding the formation of SEI layers/lithium dendrites during the lithiation/delithiation processes. $Ti_xNb_yO_z$ exhibits Wadsley–Roth shear ReO_3 crystal structures, which is different from the spinel crystal structure of $Li_4Ti_5O_{12}$[22–24]. In this structure, the Ti^{4+} and Nb^{5+} ions randomly occupy the octahedral sites, resulting in a more open crystal structure, which leads to a large Li-ion diffusion coefficient[6,23]. However, the electronic conductivity of the $Ti_xNb_yO_z$ material (<10^{-9} S cm^{-1}) is very poor due to the strong insulating characteristics of the Ti^{4+}/Nb^{5+} ions, thus restricting its rate capability[25,26]. To improve its conductivity and rate capability, it has been reported that carbon coating, graphene wrapping, or graphene hosting can efficiently enhance the rate performance of $Ti_xNb_yO_z$ materials[6,14,26]. However, studies involving $Ti_xNb_yO_z$-type anode materials in LICs are still limited. Only $TiNb_2O_7$ has been employed as an anode material in LICs, and the energy density and power density are still far from satisfying the demands of EVs and HEVs[6,27]. As a new $Ti_xNb_yO_z$ material, $TiNb_{24}O_{62}$ (TNO) exhibits a high theoretical capacity of 402 mAh g^{-1}, which is very attractive for applications in high-energy and high-power LICs[23].

Herein, we report holey graphene-wrapped porous $TiNb_{24}O_{62}$ microparticles (HG-TNO) for ultrafast pseudocapacitive lithium storage. Due to the nanoscale dimensions and hierarchically porous channels of the composite material, the ion diffusion length is shortened, and more electrochemical active sites are available, enabling fast charge/discharge rates. The as-synthesized HG-TNO material exhibits a high reversible capacity of approximately 323 mAh g^{-1} at a current of 0.1A g^{-1}, an outstanding rate capability of 183 mAh g^{-1} at a high current of 10 A g^{-1}, and an excellent cycling stability of 85% after 1000 charge/discharge cycles. Importantly, the fabricated LICs based on an HG-TNO anode and a carbon nanosheet (CN) cathode exhibit an ultrahigh energy density of 103.9 Wh kg^{-1} at a power density of 75.8 W kg^{-1}, retaining an energy density of 28.9 Wh kg^{-1} even at a high power density of 17.9 kW kg^{-1} with a high capacity retention of 81.8% after 10,000 cycles.

Experimental procedures

Porous TNO microspheres preparation

In a typical synthesis, 62 mg of TIP ($Ti(OC_3H_7)_4$, 97%) and 1.386 g of $NbCl_5$ were dissolved into 60 ml absolute ethanol with stirring for more than 30 min. Then, 0.22 ml of formic acid was added into the mixed solution and thoroughly stirred for 30 min. Next, the obtained solution was transferred to a 90 ml Teflon-lined autoclave and kept at 180 °C for 24 h. After cooling to room temperature, the precipitate was centrifuged and washed several times with ethanol. The obtained powder was dried at 80 °C and then annealed at 850 °C in air for 4 h in a tube furnace.

Holey graphene oxide preparation

The graphene oxide was synthesized by using a modified Hummers method[28]. The holey graphene oxide (HGO) was prepared by following the previously reported method with only slight modification[29]. Briefly, 40 ml of 30% H_2O_2 solution was added into 80 ml of a 10 mg ml^{-1} GO aqueous dispersion and then refluxed at 100 °C for 5 h under continuous stirring. The obtained dispersion was purified by dialysis for 5 days to remove the residual H_2O_2 and then centrifugation at 4000 rpm for 10 min to remove any aggregates. Finally, the as-prepared HGO was diluted to 3.5 mg ml^{-1} for further use.

Synthesis of HG-wrapped TNO microspheres

First, 300 mg of TNO was mixed with dopamine hydrochloride (50 mg) in 100 ml of Tris-buffer and stirred for 5 h. The obtained TNO@polydopamine microspheres were collected by centrifugation and washed several times with water and ethanol, followed by drying in an oven at 80 °C. To synthesize the HGO-wrapped TNO microsphere materials, 120 mg of TNO@PDA particles was dispersed in 50 ml of water, and then 3 ml of HGO (3.5 mg ml^{-1}) was slowly dropped into the solution and stirred for 5 h to form a cross-link between the PDA and HGO. It was then dried on a hot plate overnight under continuous stirring. Finally, the powders were calcined at 600 °C for 2 h in a protective argon atmosphere. The material was abbreviated as HG-TNO-3. For comparison, HG-TNO-5 and G-TNO were synthesized using the same method except that 5 ml of HGO (3.5 mg ml^{-1}) and 3 ml of GO (3.5 mg ml^{-1}) were added, respectively.

Synthesis of the carbon nanosheet materials

In a typical synthesis, 3.6 ml of pyrrole was dropped into 200 ml of (4 mg ml^{-1}) GO solution under stirring and then cooled down to 4 °C. Next, 5.76 g of ammonium persulfate was dissolved into 50 ml of distilled water and then added to the above solution and stirred for 20 h at 4 °C. The obtained precipitates were filtered and washed with water and ethanol. To prepare the CN material, the powder was carbonized at 600 °C for 2 h under an argon atmosphere, and it was then mixed with different mass ratios of KOH (1:4, 1:5, 1:6) and activated at various temperatures (700, 800, 900 °C) under Ar. Finally, the activated materials were washed with 5% HCl and distilled water until the solution became neutral and were dried in vacuum at 80 °C for 12 h.

Material characterization

The detailed crystal structure of TNO and HG-TNO was analyzed by X-ray diffraction (XRD, Shimadzu power diffractometer) with Cu*K*α radiation ($\lambda = 1.5406$Å). The morphology and microstructures were examined by field emission scanning electron microscopy (FESEM, JEOL 7600F) and transmission electron microscopy (TEM, JEOL 2010). Raman spectra were recorded by using a Raman spectrometer (Confocal Raman Spectrometer 633 nm). Fourier transform infrared spectrometry (FTIR) was performed in a Spectrum GX (Perkin Elmer). A Tristar II 3020 analyzer was used to measure the nitrogen adsorption/desorption isotherms and Brunauer-Emmett-Teller surface area. Thermogravimetric analyses (TGAs) were performed using a TA Q500. XPS (VG ESCA-Lab220i-XL) was performed using monochromatic Al *K*α radiation.

Electrochemical test

The electrochemical performance was evaluated in CR2032-type coin cells fabricated in an Ar-filled glove box with oxygen and water content below 0.1 ppm, 1 mol L^{-1} $LiPF_6$ in ethylene carbonate/dimethyl carbonate/diethylene carbonate (1/1/1 by volume) as the electrolyte, and microporous polypropylene membranes (Celgard 2400) as separators. The working electrodes were prepared by mixing active materials, conductive carbon, and polyvinylidene fluoride at a weight ratio of 75:15:10 to form a paste. The paste was uniformly casted onto a current collector (carbon-coated copper foils for the anode, carbon-coated alumina foils for the cathode), and then the electrodes were dried in a vacuum oven at 80 °C for 12 h. An LIC full device was also assembled in coin cells with HG-TNO as anode materials and carbon nanosheets as cathode materials, and the mass ratio between the anode and cathode was approximately 1:2.5.

All tests were carried out at room temperature. Galvanostatic charge/discharge profiles at different current densities were measured on a battery test system (Neware, China). Cyclic voltammetry (CV) and electrochemical impedance spectroscopy (EIS) were performed on an electrochemical workstation (Autolab PGSTAT30). EIS was performed with an amplitude of 5 mV in the frequency range from 100 kHz to 0.01 Hz. The voltage range was 0.8–3.0 V (vs Li/Li^+) for the anode, 2.5–4.5 V (vs Li/Li^+) for the cathode, and 1.0–3.5 V of the full LIC device. The current densities for the half cells were determined based on the mass of the active materials, and the LICs were based on both the anode and cathode active materials. The energy density (E, Wh kg^{-1}) and power density (P, Wh kg^{-1}) were calculated based on the following equations:

$$P = I \times \Delta V / m,$$
$$E = P \times t / 3600 \Delta V = V_{\max} - V_{\min},$$

where I is the constant current (A g^{-1}), t is the discharge time (s), m is the mass of active materials in both cathode and anode electrodes, $V_{\max}$ and $V_{\min}$ are the maximum and minimum working voltage during the charge/discharge process.

Results and discussion

Characterization of the HG-TNO composite

The morphology and microstructure of the as-prepared TNO precursor and the porous TNO microparticles after annealing were characterized using FESEM, as shown in Fig. 1a, b, respectively. The TNO precursor exhibits a regular spherical shape with a smooth surface. After being annealed in air, the organic species in the TNO precursor were decomposed and a porous structure was formed, which can shorten the ion diffusion length and offer more

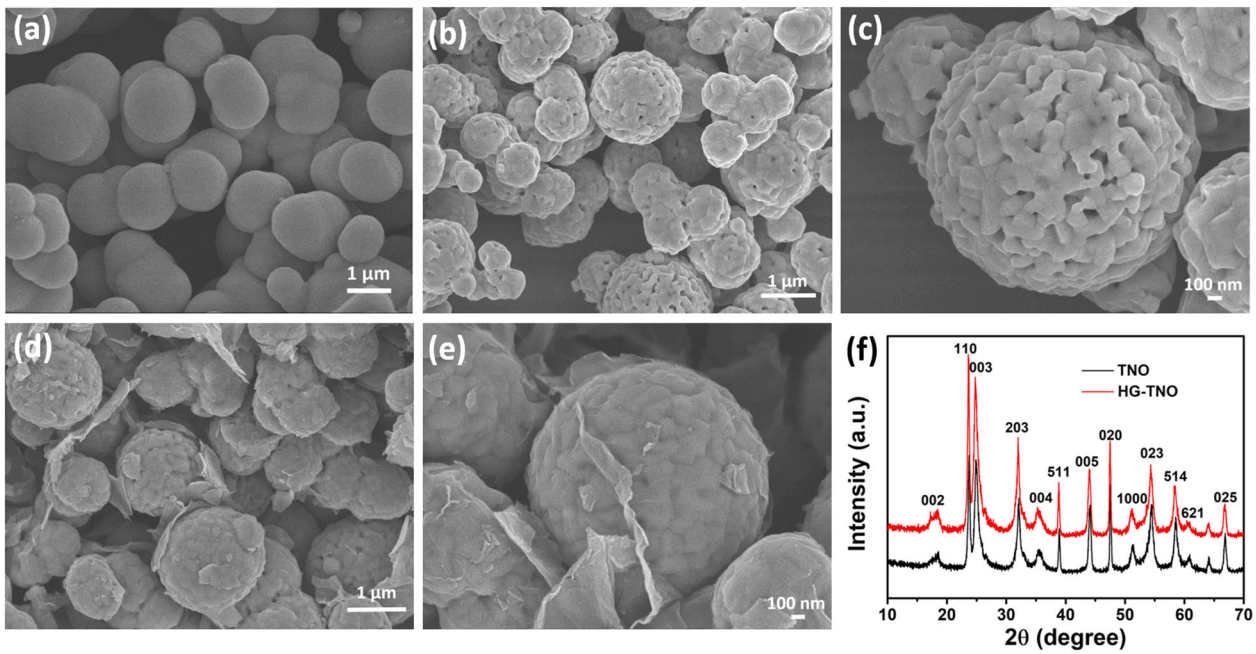

Fig. 1 Structure and morphology characterization of TNO and HG-TNO-3. a SEM image of the TNO precursor. **b**, **c** SEM images of porous TNO with different magnifications. **d**, **e** SEM images of HG-TNO-3 with different magnifications. **f** XRD patterns of TNO and HG-TNO-3

electrochemically active sites. The porous nanostructure of TNO can be clearly observed in the magnified FESEM image (Fig. 1c). The SEM images of HG-TNO are shown in Fig. 1d, e. As shown in Fig. 1d and Figure S2, almost all TNO microparticles are wrapped by holey graphene sheets. Fig. 1e shows the magnified FESEM image of HG-TNO, the crumpled holey graphene sheet can be easily distinguished on the surface of TNO, indicating the strong adhesion between the TNO and the holey graphene sheets. The XRD pattern of TNO and HG-TNO is shown in Fig. 1f. All the XRD peaks can be indexed to a perfect Wadsley–Roth shear structure with the C_2 space group[23,24]. No peaks of other crystal phases can be observed, such as TiO_2 and Nb_2O_5, indicating pure TNO was obtained. For the HG-TNO sample, no diffraction peaks can be ascribed to holey graphene, which may be attributed to the peak of holey graphene overlapping with the (110) and (003) diffraction peaks of TNO[30]. The FTIR spectra of TNO@PDA and HG-TNO-3 are shown in Figure S3. The strong bands at 1625, 1505, and 1272 cm^{-1} of TNO@PDA can be attributed to C = C or C = N, the C–H stretching band and the C–O from the catechol and amine functional groups, respectively[31,32], confirming the presence of PDA. After the carbonization, the characteristic peaks of PDA disappeared, and peaks located at 1568 and 1298 cm^{-1} were observed instead in the HG-TNO-3 sample, which can be ascribed to the C=C and C–O–C stretching in the PDA-derived N-doped carbon (N–C) and HG, indicating that PDA has been transformed into carbonaceous materials[32]. The weight ratios of TNO to carbon in HG-TNO-3 and HG-TNO-5 were studied using TGA, and the results are shown in Figure S1. The carbon content in HG-TNO-3 and HG-TNO-5 are calculated to be 5 wt% and 7.6 wt%, respectively.

The holey graphene encapsulated microparticle nanostructure is further confirmed by TEM, as shown in Fig. 2a and Figure S4a. The high-resolution TEM (HRTEM) image of HG-TNO-3 and HG-TNO-5 are shown in Fig. 2b and Figure S4b. The HRTEM images show that TNO microparticles are encapsulated with a dual-carbonaceous shell (N–C layer and HG layer), and the average thickness of the carbonaceous shell of HG-TNO-3 is less than 8.5 nm. For the HG-TNO-5 material, the average thickness is increased to 15.8 nm due to the higher content of the HG layer, which can be evidenced from the TGA result in Figure S1. As seen in Fig. 2b, the lattice spacings of 0.268 and 0.220 nm match well with the (3–15) and (914) crystallographic planes of TNO[23,30]. The hybrid nanostructure of HG-TNO can offer fast Li^+ transport and electronic transfer, enabling a high rate capability and long cycling stability. The existence of holey graphene can also be confirmed from Fig. 2c, showing the Raman spectra of TNO and HG-TNO-3. The peaks located at 546, 626, 890, and 988 cm^{-1} correspond to unique bands for TNO and are consistent with previously reported results[23,33]. In addition to the peaks for TNO, the peaks located at approximately 1357 and 1590 cm^{-1} of HG-TNO-3 are ascribed to the D band and

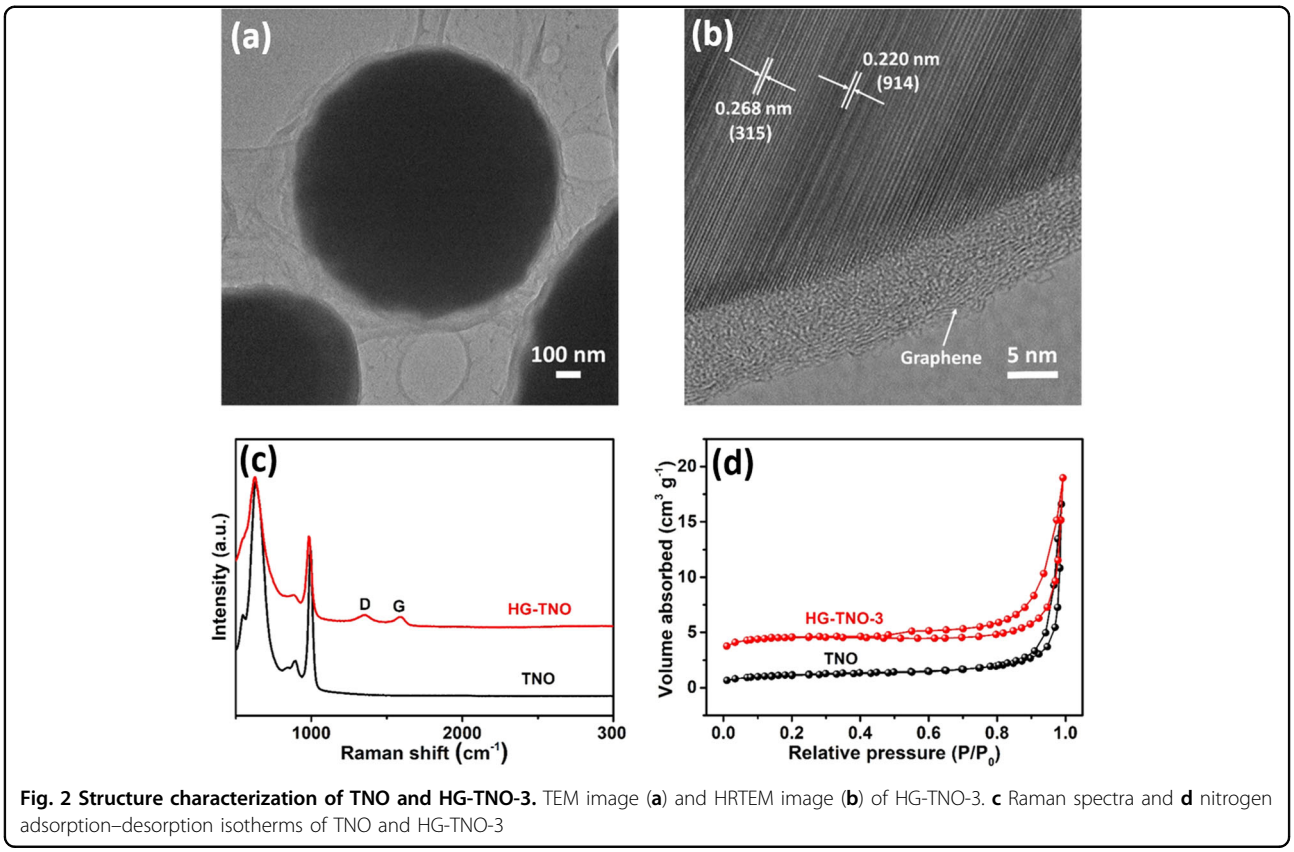

Fig. 2 Structure characterization of TNO and HG-TNO-3. TEM image (**a**) and HRTEM image (**b**) of HG-TNO-3. **c** Raman spectra and **d** nitrogen adsorption–desorption isotherms of TNO and HG-TNO-3

G band[9,14,29]. The intensity of the D band is similar to the intensity of the G band in the HG-TNO-3 composite, which may be attributed to the structural defects of holey graphene and the presence of residual oxygen groups after heat treatment[29]. Porous holey graphene can facilitate Li^+ diffusion into porous TNO, ensuring fast ionic transport due to the open ion channels. The nitrogen adsorption–desorption isotherms were tested, as shown in Fig. 2d and Figure S5a. As seen, TNO, G-TNO, HG-TNO-3, and HG exhibit a type-IV isotherm, indicating a mesoporous structure, which is in good agreement with the pore size distribution in Figure S5b[28,29] The calculated specific surface areas of TNO, HG-TNO-3, G-TNO, and HG are 4.2, 15.2, 14.7, and 95.4 $m^2 g^{-1}$, respectively. The slightly higher surface area of HG-TNO-3 than of G-TNO can be ascribed to the presence of nanoscale pores in the HG sheets. The pore size distribution of the composite materials in Figure S5b also demonstrates that HG-TNO-3 has more meso- and micropores than G-TNO. The nanoscale pores can promote ion diffusion from the electrolyte to the porous channels of TNO. Thus, the hierarchically porous channels of HG-TNO can increase the electrochemical activation sites and decrease the transport distance of the electrons/Li^+ within the particles, enhancing the electrochemical performance of the electrode materials.

Electrochemical lithium storage performance of HG-TNO composite

The electrochemical performance of the HG-TNO was evaluated using a half-cell with lithium metal as the reference and counter electrode. The potential window is between 0.8 and 3.0 V. The CV of the HG-TNO was investigated first, and the result is shown in Figure S6. The first and second cycles were different from subsequent cycles, which could be derived from the change in the electronic structure of TNO due to irreversible lithiation in the first several cycles and the irreversible lithium-ion insertion into special positions in the lattice[23,34]. This phenomenon has also been reported in other intercalation-type anode materials, such as $TiNb_2O_7$ [6,35], $Ti_2Nb_{10}O_{29}$ [14], and $TiNb_6O_{17}$[22]. After two cycles, the following CV curves almost overlapped, indicating fast reaction kinetics and an excellent cycling stability of the hybrid material. From the third cycle onwards, three pairs of cathodic/anodic peaks can be observed, and the pronounced cathodic/anodic peaks at 1.6/1.74 V can be attributed to the valence change of Nb^{5+}/Nb^{4+}[23,27]. The pair of wide shoulder peaks at 1.96/2.05 V can be assigned to the reaction of the Ti^{4+}/Ti^{3+} redox couple, while the broad bump in the potential of 0.8–1.4 V is attributed to the Nb^{4+}/Nb^{3+} redox couple[14,23]. Fig. 3a shows the rate performance of various HG-TNO

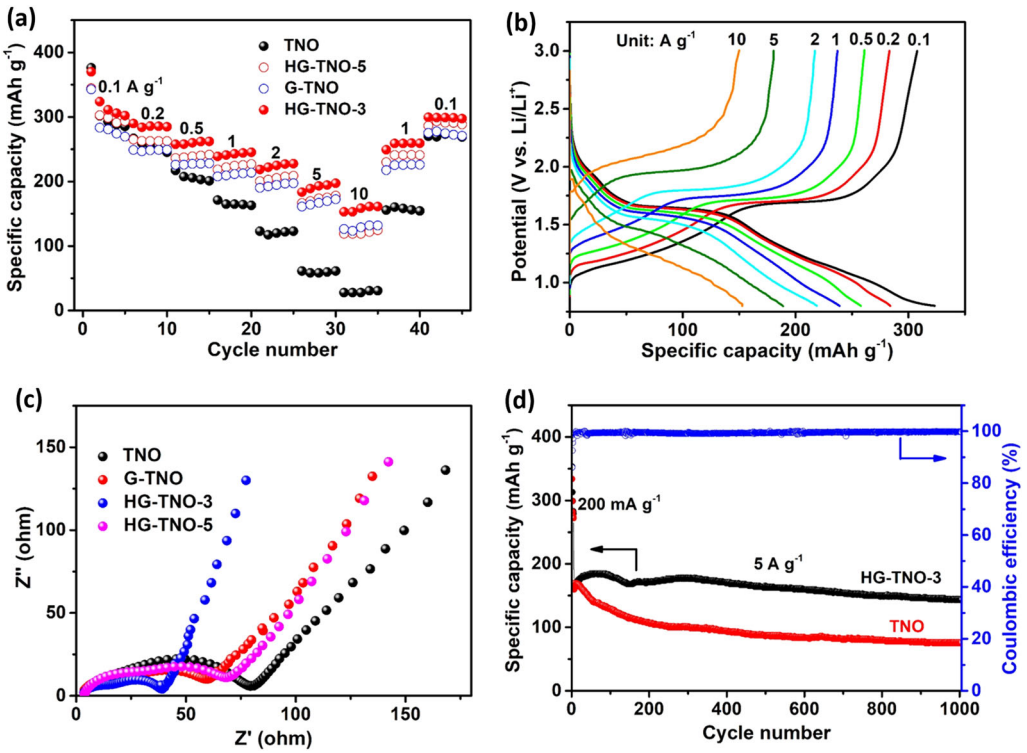

Fig. 3 Electrochemical performance of HG-TNO electrodes in the potential window of 0.8-3.0 V vs Li/Li^+. a Rate performance of HG-TNO, G-TNO, and TNO electrodes, ramping from 0.1 to 10 A g^{-1} and then back to 0.1 A g^{-1}. **b** Galvanostatic charge/discharge curves of HG-TNO-3 at different current densities. **c** Nyquist plots of the TNO, G-TNO, and HG-TNO materials. **d** Long-term cycling performance of HG-TNO-3 and TNO electrodes at 5 A g^{-1}

electrodes, a G-TNO electrode, and a pure TNO electrode. Notably, a reversible capacity of 323 mAh g^{-1} can be achieved for the HG-TNO-3 electrode at a current density of 0.1 A g^{-1}, which is higher than 301, 302, and 283 mAh g^{-1} achieved for TNO, HG-TNO-5, and G-TNO, respectively. In addition, this large reversible capacity of 323 mAh g^{-1} is greater than those of hollow $TiNb_2O_7$ nanofibers (291.7 mAh g^{-1})[27], $TiNb_2O_7$ nanoparticles (258 mAh g^{-1})[36], $Ti_2Nb_{10}O_{29}$/reduced graphene oxide (261 mAh g^{-1})[14], $Ti_{0.95}Mo_{0.05}Nb_2O_7$ nanoparticles (278 mAh g^{-1})[15], and nanoporous $TiNb_2O_7$ nanoparticles (281 mAh g^{-1})[37].

With increasing current density, HG-TNO-3 exhibits the smallest capacity decay among the four types of materials. Even at an ultrahigh current density of 10 A g^{-1}, the discharge capacity of HG-TNO-3 can still maintain a reversible capacity as high as 153 mAh g^{-1}, which is higher than those of TNO (28 mAh g^{-1}), HG-TNO-5 (118 mAh g^{-1}), and G-TNO (126 mAh g^{-1}). When the current density returned to 0.1 A g^{-1}, the specific capacity recovered to the original value after high-rate cycling, demonstrating the structural integrity of the materials. Fig. 3b shows typical charge/discharge curves of HG-TNO-3 at different current densities. To investigate the enhanced electrochemical performance of HG-TNO-3 compared with those of TNO, G-TNO, and HG-TNO-5, EIS were measured after three cycles, as shown in Fig. 3c. All the spectra show a depressed semicircle in the high-frequency regime and a vertical line in the low-frequency regime, which are related to the charge transfer resistance and solid-state diffusion of Li^+ in the electrode materials[5,10,26]. There is an obvious order to the charge transfer resistance, namely, TNO (79.3 Ω) > HG-TNO-5 (67.8 Ω) > G-TNO (59.6 Ω) > HG-TNO-3 (39 Ω), suggesting that wrapping with holey graphene and graphene can effectively reduce the charge transfer resistance of porous TNO microparticles as the highly conductive holey graphene and graphene can improve inter-particle electron conduction, resulting in enhanced electrochemical kinetics. Interestingly, HG-TNO-3 shows a smaller diameter semicircle than G-TNO, which could be attributed to facilitated Li^+ diffusion into the composite materials by the hierarchical porosity of the HG. The Li^+ ion diffusion coefficients of TNO and HG-TNO-3 were calculated from the Randles–Sevcik equation[22,37]:

$$I_p = 2.69 \times 10^5 \times n^{1.5} S C D^{0.5} V^{0.5}$$

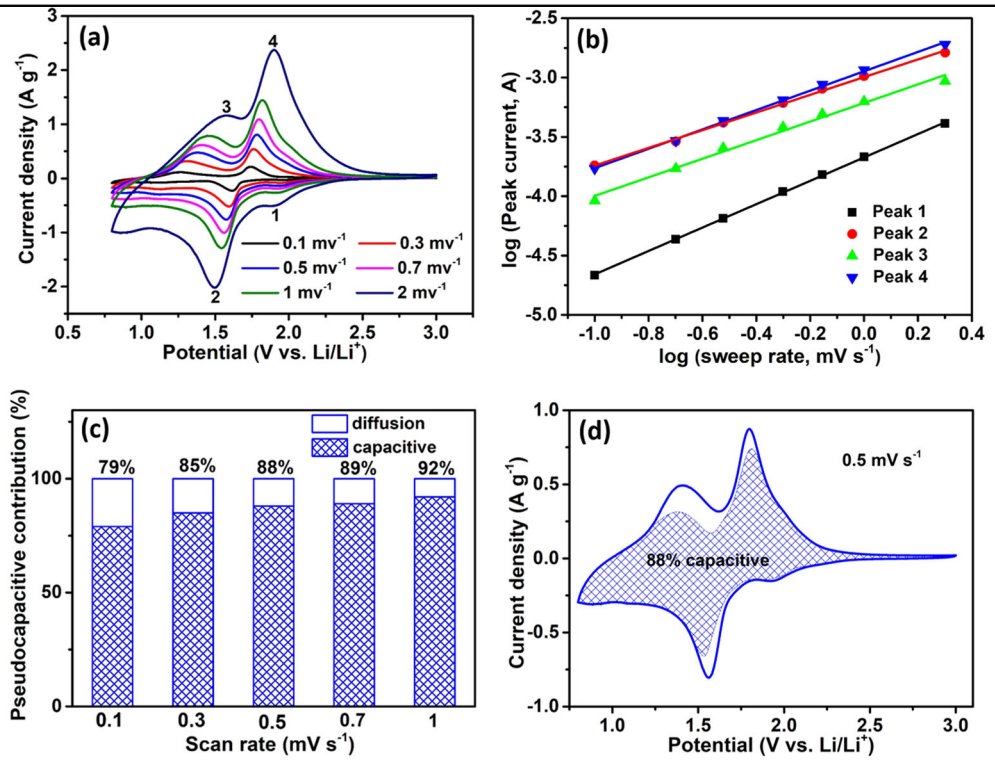

Fig. 4 Kinetics characterization of HG-TNO-3 collected in Li half-cell. a CV curves of HG-TNO-3 electrodes from 0.1 to 2 mV s^{-1}. **b** Analysis of *b* value for anodic and cathodic peaks. **c** Capacitive contribution of HG-TNO-3 electrode at different scan rates. **d** Capacitive contribution at a scan rate of 0.5 mV $^{-1}$

where *n*, *S*, and *C* are the number of electrons in the specific electrochemical reactions, surface area of the electrode (cm^2), and concentration of Li^+ ion in the solid, respectively. The calculated Li^+ ion diffusion coefficients of TNO are 7.6×10^{-13} cm^2 s^{-1}(lithiation) and 1.0×10^{-12} cm^2 s^{-1} (delithiation), and nthe Li^+ ion diffusion coefficients of HG-TNO-3 are 1.03×10^{-12} cm^2 s^{-1} (lithiation) and 1.3×10^{-12} cm^2 s^{-1} (delithiation), which are larger than those of $TiNb_6O_{17}$ (5.48×10^{-14} and 4.28×10^{-14} cm^2 s^{-1}) and $Ti_2Nb_{14}O_{29}$ (9.07×10^{-14} and 5.52×10^{-14} cm^2 s^{-1})[22,38]. The large value of TNO and HG-TNO-3 can be explained by the porous structure that can provide facile Li^+ ion transport pathways and shorter ion diffusion length, facilitating the Li^+ ion transport during the charge and discharge processes. The higher Li^+ ion diffusion coefficient of HG-TNO-3 than TNO indicates that the highly porous HG connecting individual TNO microparticles can promote Li^+ ion. The calculated Li^+ ion diffusion coefficients of HG-TNO-5 are 9.3×10^{-13} (lithiation) and 1.2×10^{-12} cm^2 s^{-1} (delithiation), which are smaller than those of the HG-TNO-3 due to the thicker HG layer on TNO microparticles. The thick HG layer will increase the Li^+ ion diffusion length, which agrees well with the HRTEM of HG-TNO-3 and HG-TNO-5 in Fig. 2b and S4b.

After being activated at a current of 0.2 A g^{-1} for five cycles, the long-term cycling stability of HG-TNO-3 and TNO at a high current of 5 Ag^{-1} was investigated. As shown in Fig. 3d, a reversibly capacity of 143 mAh g^{-1} was maintained after 1000 cycles with a capacity retention of approximately 85.1%, which is higher than that of pure TNO (44.3%). The coulombic efficiency was approximately 100% after few cycles. The enhanced rate performance and cycling stability of HG-TNO-3 is attributed to the presence of HG, which can not only improve the conductivity of TNO but also favor ion transport.

Lithium storage mechanism in HG-TNO material

To further investigate the electrochemical storage mechanism of the HG-TNO-3 electrode, CV curves at different scan rates between 0.8 and 3.0 V were recorded (Fig. 4a). As shown in Fig. 4a, two reduction peaks and two oxidation peaks distinctly exist in each cycle, with an increase in current density exhibited as the scan rates were raised. The CV curves of HG-TNO-3 at higher scan rates are also presented in the supporting information, as shown in Figure S7a. At much higher scan rates, the redox peaks were still maintained with increased current density. According to previous studies, the peak current (*i*) of the CV curves obeys a power-law relationship with the

scan rate (v) and can be used to analyze the charge storage mechanism from the following equation[2,4,39,40]:

$$i = \alpha v^b$$

where i and v are the peak current and scan rate, respectively, and α and b are adjustable parameters. If $b = 1$, the electrochemical system shows pseudocapacitive behavior controlled by a surface faradic reaction[6,40]. If $b = 0.5$, typical ionic diffusion dominates the charge/discharge process by cation intercalation[6,39]. The plots of log (i) vs log(v) for both the anodic and cathodic peaks are shown in Fig. 4b and Figure S7b. With the scan rates ranging from 0.1 to 2 mV s^{-1}, the peak current increases linearly with the increase in scan rate. The b-values for the peaks of 1, 2, 3, and 4 are 0.82, 0.75, 0.78, and 0.99, respectively, indicating that the redox processes of HG-TNO-3 are dominated by pseudocapacitive kinetics. At higher scan rates of 5–100 mV s^{-1}, the b-values decrease to 0.58 for the anodic current and 0.54 for the cathodic current, demonstrating the dominance of the diffusion-controlled process. These results undoubtedly confirm the pseudocapacitive behavior of HG-TNO-3, leading to fast Li^+ intercalation/extraction and excellent long-term cycling stability, demonstrating the material's suitability as an anode material for high-power LICs. To quantitatively distinguish the capacitive contribution from the current response through the voltammetric scan rate, the equation can be rewritten as[2,38,39]

$$i = k_1 v + k_2 v^{1/2},$$

where k_1 and k_2 are constants. The current at a fixed potential is a combination of capacitive effects ($k_1 v$) and diffusion contributions ($k_2 v^{1/2}$). By plotting $i/v^{1/2}$ vs $v^{1/2}$, k_1 and k_2 are calculated from the slope and the y-axis intercept point of a straight line, respectively[2,4,39]. The ratio of the pseudocapacitive contribution at various scan rates can be quantitatively determined, and the results are shown in Fig. 4c. The pseudocapacitive contributions of HG-TNO-3 are 79%, 85%, 88%, 89%, and 92% at scan rates of 0.1, 0.3, 0.5, 0.7, and 1 mV s^{-1}, respectively. It can be found that with the increase in scan rates, the capacitive contribution further increases. The detail of the pseudocapacitive fraction at a scan rate of 0.5 mV s^{-1} was plotted in Fig. 4d, and 88% of the total charge comes from capacitive processes. The high capacitive contribution is attributed to the short ion diffusion length and rapid electron transfer of the HG-TNO-3 electrode, which leads to an unprecedented high rate and long-term cycling performance.

Ex situ XRD analysis was performed to study the lithiation/delithiation mechanism of HG-TNO-3 materials, as shown in Figure S8. These XRD patterns are very similar despite small variations in the peak intensities and positions, indicating that the crystal structures were maintained during the entire electrochemical testing process, albeit with small volume variations. After lithiation, the peak positions of the HG-TNO-3 discharged to 0.8 V negatively shifted to smaller Bragg angles, indicating small lattice expansion caused by Li-ion insertion into TNO. After being charged back to 3.0 V, these Bragg reflections recovered to the initial diffraction angles, indicating the small volume change and good reversibility, which aligns with the intercalation-based electrochemical mechanism of TNO as well as its excellent cycling stability. In addition, the ex situ XPS spectra of Nb in TNO have been captured for analyzing the corresponding valence evolution during the electrochemical process, and the result is shown in Figure S9. In the initial electrode material, the binding energies at approximately 207.6 and 210.3 eV are indicative of Nb $3d_{5/2}$ and Nb $3d_{3/2}$ of Nb^{5+}, respectively, associated with pristine TNO[5]. After being discharged to 0.8 V, four new peaks located at 203.7, 205.7, 206.4, and 208.4 eV were noticed, which are typical of the $3d_{5/2}$ and $3d_{3/2}$ of Nb^{3+} (203.7, 206.4 eV) and Nb^{4+} (205.7, 208.4 eV), respectively, indicating the reduction of Nb^{5+} during the discharging process upon lithiation[41,42].

In addition, ex situ TEM selected area electron diffraction patterns of HG-TNO-3 before and after the discharge process were also collected, as in Figure S6. As seen from Figure S6a, the diffraction spots of pristine TNO can be ascribed to the crystal planes of (110), (203), and (020), with d-spacings of 0.364, 0.287, and 0.192 nm, respectively. After being discharged, the diffraction spots can be indexed to the slightly expanded crystal planes of (110), (203), and (023), with d-spacings of 0.377, 0.292, and 0.169 nm, respectively. The slight increase in the d-spacing of TNO in the discharge process upon lithiation aligns with the ex situ XRD observations, explaining the excellent cycling stability of TNO based on the intercalation mechanism.

Assembly and electrochemical performance of lithium-ion capacitors

Based on the excellent electrochemical performance of HG-TNO-3 in the half-cell test, it is necessary to fabricate a full LIC cell to demonstrate the practical applications. To construct a high-performance LIC, a suitable cathode material with comparable capacitance should be developed to couple with the HG-TNO-3 anode. In this work, CN was synthesized using GO-polypyrrole as a precursor, and the carbonated temperature and mass ratio with KOH were optimized (Figures S7–S10, Table S1). The CN material with a carbonation temperature of 800 °C and a KOH/CN ratio of 5:1 exhibited the best result. The CN material can deliver a high capacity of 91.7 mAh g^{-1} at the current density of 0.2 A g^{-1}, and the capacity can maintain 44.2 mAh g^{-1} at a high current density of 10 A g^{-1} (Figure S10). By using this CN material as a cathode and

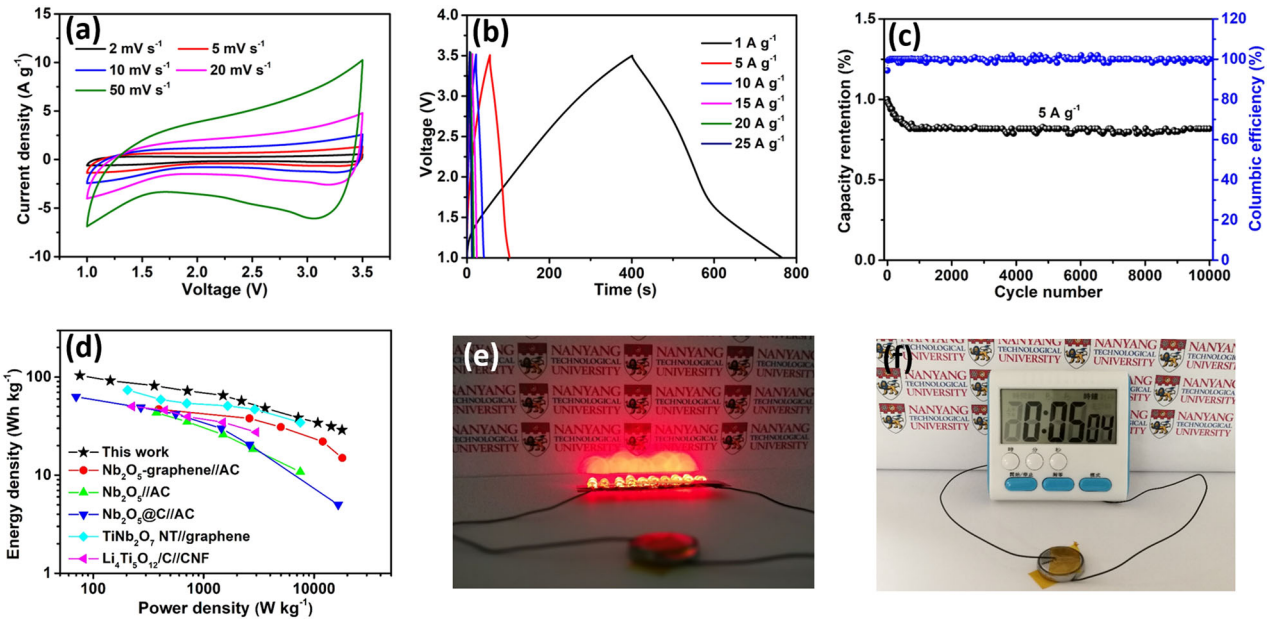

Fig. 5 Electrochemical performance of the full LIC device. a CV curves of HG-TNO-3//CN LIC from 2 to 50 mV^{-1}. **b** Galvanostatic charge/discharge curves of the HG-TNO-3//CN LIC from 1 to 25 Ag^{-1}. **c** Long-term cycling performance of the LIC at 5 A g^{-1}. **d** Ragone plots of the LIC vs the other reported LICs: Nb_2O_5-graphene//AC[30], Nb_2O_5//AC[20], Nb_2O_5@C//AC[21], $TiNb_2O_7$ NT//graphene[27], $Li_4Ti_5O_{12}$/C//CNF[7]. **e** A demo of the illumination of 10 red LEDs by a charged LIC. **f** A demo of the timer powered by a charged LIC

the HG-TNO-3 material as an anode, a full LIC was fabricated.

During the charging process, PF_6^- ions rapidly adsorb on the surface of CN, and Li^+ ions rapidly intercalate into the HG-TNO-3 electrode. To avoid the risks of electrolyte decomposition and side reactions, the working voltage window of the cell was controlled between 1.0 and 3.5 V. Considering the capacity and working potential of the electrode, the weight ratio of the cathode to anode was controlled to be 2.5:1. As shown in Fig. 5a, the CV curves of the LIC at different scan rates between 2 and 50 mV s^{-1} with the working voltage of 1.0–3.5 V exhibited a nearly quasi-rectangular shape at all scan rates, indicating that the fast Li^+ intercalation of HG-TNO-3 can match the rapid PF_6^- adsorption on the CN surface. In addition, by increasing scan rates, the shape of the CV curves can be well maintained without deviation, showing the excellent combination between the intercalation reaction anode and the non-faradaic capacitive charge storage cathode materials. This result indicates that the HG-TNO-3 electrode can be used as a high-power anode material for LICs due to the pseudocapacitive behavior. Fig. 5b displays the typical galvanostatic charge/discharge curves from 1 to 25 A g^{-1}. The charge/discharge curves of the LIC exhibit a nearly symmetric quasi-triangular shape, unlike those of the symmetric SC, indicating two different energy storage mechanisms for the anode and cathode materials, which is in good agreement with the CV results. The long-term cycling stability of the LIC was studied using the galvanostatic charge/discharge measurement at a current density of 5 A g^{-1}, and the result is shown in Fig. 5c. The capacity slightly decreases in the first 500 cycles, and then, a capacity of 81.8% of its initial value after 10,000 cycles as well as a high coulombic efficiency at round 100% during the cycling measurement was maintained, demonstrating the excellent reversibility of the LIC.

Based on the galvanostatic charge/discharge results, the energy and power density of the device based on the total mass of both electrodes can be calculated, and the Ragone plot is shown in Fig. 5d. At a low power density of 75.8 W kg^{-1}, the LIC achieved a high energy density of 103.9 Wh kg^{-1}, which is higher than the maximum energy density values of Nb_2O_5@C//AC LIC (63 Wh kg^{-1})[21], $TiNb_2O_7$ nanotubes//graphene LIC (74 Wh kg^{-1})[27], and Nb_2O_5-graphene//AC (47 Wh kg^{-1})[30]. Even at the ultra-high power density of 17.9 kW kg^{-1}, which is approaching the target for EVs[4,10], it can still deliver an energy density of 28.9 Wh kg^{-1}, demonstrating its excellent rate performance. These results indicate that this LIC can bridge the gap between LIBs and SCs to possess both high energy density and high power density. The energy and power densities of reported LICs using pseudocapacitive anode materials, such as Nb_2O_5@C//AC[21], $TiNb_2O_7$ nanotubes//graphene[27], Nb_2O_5-graphene//AC[30], $TiNb_2O_7$@C//CFs[6], and MoS_2//AC[42], are listed in Table S2

for comparison. The exceptional electrochemical performance of the LIC is related to the following features of the composite materials. First, compared with graphene, the holey graphene-wrapped porous TNO microparticles can provide both high electronic and ionic transport[9,29]. Second, the porous structure of TNO can maximize exposure of the electrochemically active sites for fast surface/near-surface charge storage and can reduce lithium transport distance in the solid state[23,35]. Third, the TNO Wadsley–Roth shear structure induced the pseudocapacitive Li^+ intercalation characteristics present in the HGO-TNO material to provide a greater capacity and a high rate performance as well as long-term cycling stability[25,43]. Fourth, the high capacity and excellent rate capability of the prepared CN cathode material also contributed greatly to the superior performance of the LIC. To demonstrate the HG-TNO-3//CN LIC device in practical applications, a single LIC device can power 10 red light-emitting diodes (LEDs) for more than 15 min after being charged for 90 s (Fig. 5e) and can also power a commercial timer after being charged (Fig. 5f). These results demonstrate the great promise of our LIC as both a high energy and high power density source for HEVs and EVs.

Conclusions

In summary, we developed a HG-wrapped TNO composite as a pseudocapacitive material for electrochemical Li^+ storage, exhibiting a high rate capacity, high specific capacity, and excellent cycling stability. By taking advantage of the synergistic effects of TNO with a high capacity and HG with a high electronic/ionic conductivity, the composite can deliver a reversible capacity of 323 mAh g^{-1} at a current density of 0.1 A g^{-1}, even at a high current density of 10 A g^{-1}, the capacity can still maintain approximately 153 mAh g^{-1}. By coupling with a CN-based cathode, the as-fabricated LIC exhibited a high energy density of 103.9 Wh kg^{-1} at a power density of 75.8 W kg^{-1}, and the energy density was maintained at 28.9 Wh kg^{-1} at a high output power of 17.9 kW kg^{-1}. Moreover, over 81.8% of the capacity can be retained after 10,000 cycles. This work demonstrates an excellent lithium-based energy storage device with both high energy and power densities as well as long-term stability, showing its potential as a promising candidate for highly efficient energy storage systems.

Acknowledgements
This work was financially supported by the NRF Investigatorship (NRFI), Award No. NRF-NRFI2016-05 and Ministry of Education Tier 2 Grant, Award No. MOE2015-T2-1-129.

Conflict of interest
The authors declare that they have no conflict of interest.

Supplementary information is available for this paper at https://doi.org/10.1038/s41427-018-0042-5.

Received: 17 December 2017 Revised: 12 February 2018 Accepted: 6 March 2018.
Published online: 22 May 2018

References

1. Salanne, M. et al. Efficient storage mechanisms for building better supercapacitors. *Nat. Energy* **1**, 16070 (2016).
2. Augustyn, V. et al. High-rate electrochemical energy storage through Li^+ intercalation pseudocapacitance. *Nat. Mater.* **12**, 518–522 (2013).
3. Armand, M. & Tarascon, J.-M. Building better batteries. *Nature* **451**, 652–657 (2008).
4. Augustyn, V., Simon, P. & Dunn, B. Pseudocapacitive oxide materials for high-rate electrochemical energy storage. *Energy Environ. Sci.* **7**, 1597–1614 (2014).
5. Li, S. et al. Freestanding bacterial cellulose–polypyrrole nanofibres paper electrodes for advanced energy storage devices. *Nano Energy* **9**, 309–317 (2014).
6. Wang, X. & Shen, G. Intercalation pseudo-capacitive $TiNb_2O_7$@carbon electrode for high-performance lithium ion hybrid electrochemical supercapacitors with ultrahigh energy density. *Nano Energy* **15**, 104–115 (2015).
7. Xu, H. et al. Highly porous $Li_4Ti_5O_{12}$/C nanofibers for ultrafast electrochemical energy storage. *Nano Energy* **10**, 163–171 (2014).
8. Won, J. H., Jeong, H. M. & Kang, J. K. Synthesis of nitrogen-rich nanotubes with internal compartments having open mesoporous channels and utilization to hybrid full-cell capacitors enabling high energy and power densities over robust cycle life. *Adv. Energy Mater.* **7**, 1601355 (2017).
9. Zhang, F. et al. A high-performance supercapacitor-battery hybrid energy storage device based on graphene-enhanced electrode materials with ultrahigh energy density. *Energy Environ. Sci.* **6**, 1623–1632 (2013).
10. Li, S. et al. A high-performance lithium-ion capacitor based on 2D nanosheet materials. *Small* **13**, 1602893 (2017).
11. Chou, S.-L., Wang, J.-Z., Liu, H.-K. & Dou, S.-X. Rapid synthesis of $Li_4Ti_5O_{12}$ microspheres as anode materials and its binder effect for lithium-ion battery. *J. Phys. Chem. C* **115**, 16220–16227 (2011).
12. Yu, L., Wu, H. B. & Lou, X. W. Mesoporous $Li_4Ti_5O_{12}$ hollow spheres with enhanced lithium storage capability. *Adv. Mater.* **25**, 2296–2300 (2013).
13. Heenen, H. H., Scheurer, C. & Reuter, K. Implications of occupational disorder on ion mobility in $Li_4Ti_5O_{12}$ battery materials. *Nano Lett.* **17**, 3884–3888 (2017).
14. Wang, W. L. et al. Solid-state synthesis of $Ti_2Nb_{10}O_{29}$/reduced graphene oxide composites with enhanced lithium storage capability. *J. Power Sources* **300**, 272–278 (2015).
15. Song, H. & Kim, Y. T. A Mo-doped $TiNb_2O_7$ anode for lithium-ion batteries with high rate capability due to charge redistribution. *Chem. Commun.* **51**, 9849–9852 (2015).
16. Liu, H. et al. Mesoporous TiO_2-B microspheres with superior rate performance for lithium ion batteries. *Adv. Mater.* **23**, 3450–3454 (2011).
17. Cao, M., Gao, L., Lv, X. & Shen, Y. TiO_2-B@VS_2 heterogeneous nanowire arrays as superior anodes for lithium-ion batteries. *J. Power Sources* **350**, 87–93 (2017).
18. Gao, L., Li, S., Huang, D., Shen, Y. & Wang, M. Porous $Li_4Ti_5O_{12}$–TiO_2nanosheet arrays for high-performance lithium-ion batteries. *J. Mater. Chem. A* **3**, 10107–10113 (2015).
19. Kong, L. et al. Nanoarchitectured Nb_2O_5 hollow, Nb_2O_5@carbon and NbO_2@carbon core-shell microspheres for ultrahigh-rate intercalation pseudocapacitors. *Sci. Rep.* **6**, 21177 (2016).
20. Wang, X., Yan, C., Yan, J., Sumboja, A. & Lee, P. S. Orthorhombic niobium oxide nanowires for next generation hybrid supercapacitor device. *Nano Energy* **11**, 765–772 (2015).
21. Lim, E. et al. Facile synthesis of Nb_2O_5@ carbon core–shell nanocrystals with controlled crystalline structure for high-power anodes in hybrid supercapacitors. *ACS Nano* **9**, 7497–7505 (2015).

22. Lin, C., Wang, G., Lin, S., Li, J. & Lu, L. $TiNb_6O_{17}$: a new electrode material for lithium-ion batteries. *Chem. Commun.* **51**, 8970–8973 (2015).
23. Yang, C. et al. Porous $TiNb_{24}O_{62}$ microspheres as high-performance anode materials for lithium-ion batteries of electric vehicles. *Nanoscale* **8**, 18792–18799 (2016).
24. Wadsley, A. Mixed oxides of titanium and niobium. I. *Acta Cryst.* **14**, 660–664 (1961).
25. Liu, G. et al. Synthesis of $Ti_2Nb_{10}O_{29}$/C composite as an anode material for lithium-ion batteries. *Int. J. Hydro. Energy* **41**, 14807–14812 (2016).
26. Li, S. et al. $TiNb_2O_7$/graphene composites as high-rate anode materials for lithium/sodium ion batteries. *J. Mater. Chem. A* **4**, 4242–4251 (2016).
27. Li, H. et al. Three-dimensionally ordered porous $TiNb_2O_7$nanotubes: a superior anode material for next generation hybrid supercapacitors. *J. Mater. Chem. A* **3**, 16785–16790 (2015).
28. Chen, J., Wang, X., Wang, J. & Lee, P. S. Sulfidation of NiMn-layered double hydroxides/graphene oxide composites toward supercapacitor electrodes with enhanced performance. *Adv. Energy Mater.* **6**, 1501745 (2016).
29. Xu, Y. et al. Solution processable holey graphene oxide and its derived macrostructures for high-performance supercapacitors. *Nano Lett.* **15**, 4605–4610 (2015).
30. Kong, L. et al. Free-standing T-Nb_2O_5/graphene composite papers with ultrahigh gravimetric/volumetric capacitance for li-ion intercalation pseudocapacitor. *ACS Nano* **9**, 11200–11208 (2015).
31. Li, R., Parvez, K., Hinkel, F., Feng, X. & Klaus, M. Bioinspired wafer-scale production of highly stretchable carbon films for transparent conductive electrodes. *Angew. Chem.* **125**, 5645–5648 (2013).
32. Li, h. et al. Facile synthesis of N-doped carbon-coated $Li_4Ti_5O_{12}$ microspheres using polydopamine as a carbon source for high rate lithium ion batteries. *J. Mater. Chem. A* **1**, 7270–7276 (2013).
33. Cheng, Q. et al. Porous $TiNb_2O_7$ nanospheres as ultra long-life and high-power anodes for lithium-ion batteries. *Electrochim. Acta* **176**, 456–462 (2015).
34. Lu, X. et al. Atomic-scale investigation on lithium storage mechanism in $TiNb_2O_7$. *Energy Environ. Sci.* **4**, 2638–2644 (2011).
35. Park, H., Song, T. & Paik, U. Porous $TiNb_2O_7$ nanofibers decorated with conductive $Ti_{1-x}Nb_xN$ bumps as a high power anode material for Li-ion batteries. *J. Mater. Chem. A* **3**, 8590–8596 (2015).
36. Li, H. et al. $TiNb_2O_7$ nanoparticles assembled into hierarchical microspheres as high-rate capability and long-cycle-life anode materials for lithium ion batteries. *Nanoscale* **7**, 619–624 (2015).
37. Guo, B. et al. A long-life lithium-ion battery with a highly porous $TiNb_2O_7$ anode for large-scale electrical energy storage. *Energy Environ. Sci.* **7**, 2220 (2014).
38. Lin, C. et al. Intercalating $Ti_2Nb_{14}O_{39}$ anode materials for fast-charging, high-capacity and safe lithium-ion batteries. *Small* **13**, 1702903 (2017).
39. Kim, J. W., Augustyn, V. & Dunn, B. The effect of crystallinity on the rapid pseudocapacitive response of Nb2O5. *Adv. Energy Mater.* **2**, 141–148 (2012).
40. Wang, X. & Lee, P. S. Titanium doped niobium oxide for stable pseudocapacitive lithium ion storage and its application in 3 V non-aqueous supercapacitors. *J. Mater. Chem. A* **3**, 21706–21712 (2015).
41. Tabata, K., Kamada, M., Choso, T. & Munakata, H. Photoelectron spectroscopy investigation of NO adsorption on defects of $LiNbO_3$ surfaces. *Appl. Surf. Sci.* **125**, 93–98 (1998).
42. Cook, J. B. et al. Pseudocapacitive charge storage in thick composite MoS_2 nanocrystal-based electrodes. *Adv. Energy Mater.* **7**, 1601283 (2017).
43. Noh, H. & Choi, W. Preparation of a $TiNb_2O_7$ microsphere using formic acid and wrapping with reduced graphene oxide for anodes in lithium ion batteries. *J. Electrochem. Soc.* **163**, A1042–A1049 (2016).